Journal of Geophysical Research: Oceans

RESEARCH ARTICLE
10.1029/2017JC013584

Special Section:
Oceanic Responses and Feedbacks to Tropical Cyclones

Generation of Near-Inertial Currents on the Mid-Atlantic Bight by Hurricane Arthur (2014)

Fan Zhang[1], Ming Li[1], and Travis Miles[2]

[1]Horn Point Lab, University of Maryland Center for Environmental Science, Cambridge, Maryland, USA, [2]Department of Marine and Coastal Sciences, Center for Ocean Observing Leadership, Rutgers University, New Brunswick, New Jersey, USA

Abstract Near-inertial currents (NICs) were observed on the Mid-Atlantic Bight (MAB) during the passage of Hurricane Arthur (2014). High-frequency radars showed that the surface currents were weak near the coast but increased in the offshore direction. The NICs were damped out in 3–4 days in the southern MAB but persisted for up to 10 days in the northern MAB. A Slocum glider deployed on the shelf recorded two-layer baroclinic currents oscillating at the inertial frequency. A numerical model was developed to interpret the observed spatial and temporal variabilities of the NICs and their vertical modal structure. Energy budget analysis showed that most of the differences in the NICs between the shelf and the deep ocean were determined by the spatial variations in wind energy input. In the southern MAB, energy dissipation quickly balanced the wind energy input, causing a rapid damping of the NICs. In the northern MAB, however, the dissipation lagged the wind energy input such that the NICs persisted. The model further showed that mode-1 waves dominated throughout the MAB shelf and accounted for over 70% of the current variability in the NICs. Rotary spectrum analyses revealed that the NICs were the largest component of the total kinetic energy except in the southern MAB and the inner shelf regions with strong tides. The NICs were also a major contributor to the shear spectrum over an extensive area of the MAB shelf and thus may play an important role in producing turbulent mixing and cooling of the surface mixed layer.

Key Points:
- Spatial variations of near-inertial currents generated by Hurricane Arthur were mostly related to wind energy input
- The balance between wind energy input and dissipation determined the damping or persistence of near-inertial currents
- Mode-1 near-inertial waves contained over 70% of the kinetic energy and were a major contributor to the current shear

Correspondence to:
F. Zhang,
fzhang@umces.edu

Citation:
Zhang, F., Li, M., & Miles, T. (2018). Generation of near-inertial currents on the Mid-Atlantic Bight by Hurricane Arthur (2014). *Journal of Geophysical Research: Oceans*, *123*, 3100–3116. https://doi.org/10.1029/2017JC013584

Received 26 OCT 2017
Accepted 2 APR 2018
Accepted article online 6 APR 2018
Published online 30 APR 2018

1. Introduction

When a tropical or an extratropical storm moves over the deep ocean, wind stress fluctuations at frequencies in the near-inertial band can resonantly force inertial currents in the surface mixed layer. Pollard and Millard (1970) and Pollard (1980) found that up to two-thirds of the kinetic energy in the mixed layer is contained within the near-inertial band during storms. The ocean response to a hurricane can be separated into two stages. The "forced" stage response during the storm passage includes strong mixed-layer currents and rapid cooling of the sea surface temperature (Cuypers et al., 2013; D'Asaro et al., 2007; Sanford et al., 2007, 2011). Price et al. (1994) used a three-dimensional model to simulate the forced stage response to three hurricanes and found that the near-inertial currents (NICs) have a rightward bias due to the coupling between the clockwise-rotating wind stress and mixed-layer currents on the right side of the track. The "relaxation stage" response after the storm passage involves the dispersion of near-inertial frequency internal waves into the stratified interior of the ocean (Gill, 1984; Price, 1983). Gill (1984) developed a modal model to describe the excitation of submixed-layer motions by a passing storm and found that the energy projects predominantly on the lowest modes. The horizontal scale of the near-inertial waves is initially set by the scales of wind stress in the storm (Gill, 1984; Price, 1983). Several processes act to decrease the horizontal scales of the mixed-layer motions, generating shorter waves that can propagate into the stratified interior (Alford et al., 2016). In particular, D'Asaro et al. (1995) and D'Asaro (1995a, 1995b) demonstrated the role of the latitude-dependent Coriolis parameter or the β effect in reducing the horizontal scales of the near-inertial waves.

When a storm moves over the continental shelf, however, its wind stress and wind stress curl may excite several different modes of oceanic variability besides the near-inertial waves. Longshore winds could generate upwelling or downwelling along the coast. Onshore winds may drive onshore surface currents and offshore bottom currents, and the resulting shear-induced mixing could lead to rapid ahead-of-eye center cooling of the surface mixed layer (Glenn et al., 2016; Seroka et al., 2016, 2017). Nevertheless, Chen et al.

(1996) and Chant (2001) reported observations of low-mode near-inertial internal waves that are consistent with local wind forcing. Shearman (2005) analyzed 1 year long observations from the Coastal Mixing and Optics moored array on the New England shelf, and found that a mode-1 baroclinic structure was coherent across the entire shelf, with a magnitude that decreased onshore. This onshore decrease of NICs is consistent with the theoretical prediction of a two-dimensional, linear, flat-bottom, two-layer, coastal wall model by Pettigrew (1981). The presence of a coastal boundary causes divergence in the surface mixed layer, generating NICs below it and leading to low modal wave structure. Shearman (2005) also observed that the near-inertial waves were stronger in the summer and weaker in the winter, following the seasonal cycle in vertical stratification but opposite to the seasonal change in wind stress. MacKinnon and Gregg (2005) analyzed the mooring data collected during the spring stratification period and tracked the generation, evolution and decay of the near-inertial waves. They found that the wave evolution was controlled by the balance among wind stress, bottom drag, and turbulent dissipation. Moreover, they observed a switch from mode-1 to mode-2 waves as the stratification evolved, and attributed the switch to nonlinear coupling of the waves through bottom stress.

Although these previous studies have yielded important insights into the structure and dynamics of near-inertial waves on the continental shelf, the coastal ocean response to a passing storm is not completely understood. The mooring observations described above provided detailed time series at a few sites but could not provide a synoptic picture of the shelf-wide response to a storm. It is not clear if the NICs, which dominate the ocean response to storms in the deep ocean, remain to be an important part of the storm-induced currents on the shelf. Neither is it clear if the shear associated with NICs contributes to turbulent mixing and the cooling of the surface mixed layer that may reduce the storm intensity.

Hurricane Arthur (2014) provides a unique opportunity to document and analyze the coastal ocean response to a tropical storm. Arthur moved over the Mid-Atlantic Bight (MAB) on 4 July 2014, after making landfall in North Carolina and re-entering the North Atlantic (Figure 1). Arthur attained a maximum

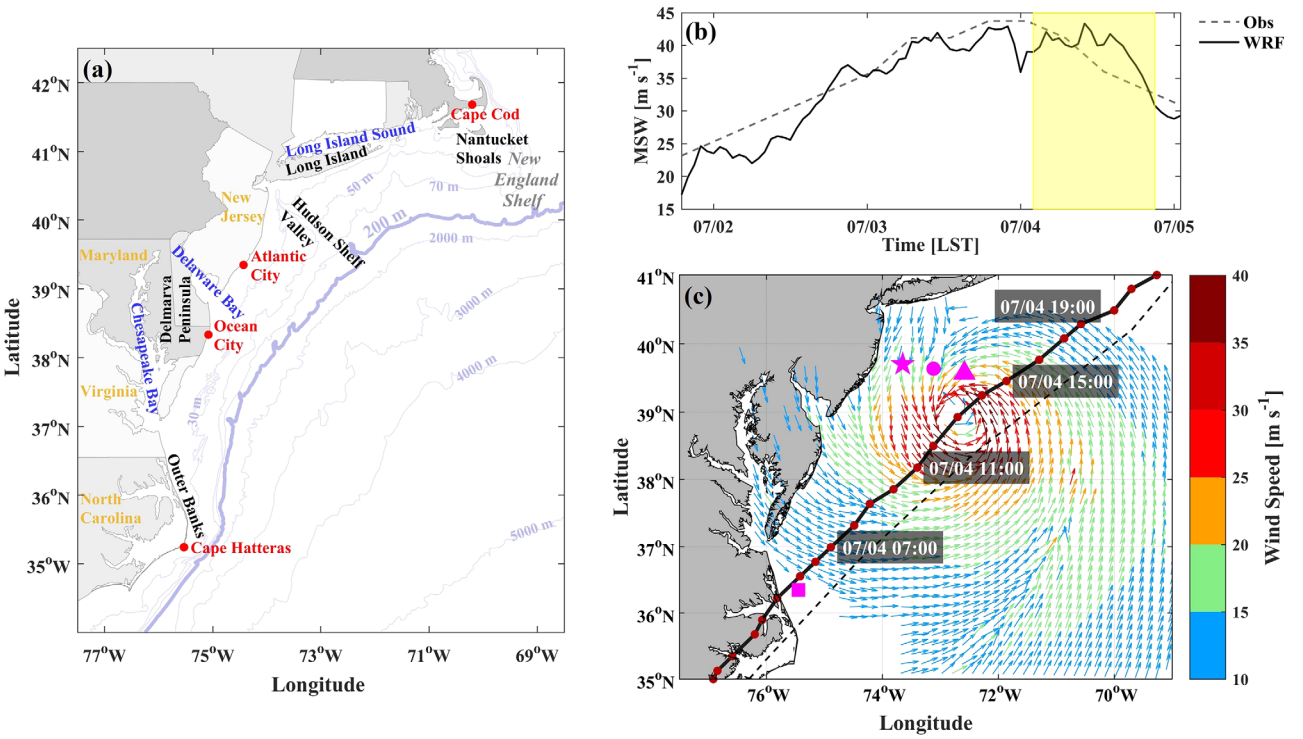

Figure 1. (a) Map and bathymetry of the MAB. Water depth drops sharply beyond the 200 m isobath. (b) Time series of the WRF-predicted (solid) and observed (dashed) maximum sustained winds (MSW) at 10 m height during the passage of Hurricane Arthur. The shaded area indicates the time period of Arthur's passage over the MAB. (c) Predicted surface winds at 13:00 LST 4 July. Wind speeds lower than 10 m s^{-1} are not shown. The black solid line with timestamps (red dots spaced at the interval of 1 h) represents the predicted storm track, and the black dashed line represents the observed track. The magenta triangle marks Buoy 44066, the magenta star marks the approximate location of the glider, and magenta dot and square mark the third and fourth locations used for the rotary spectrum analysis in Figure 3, respectively.

sustained wind (MSW) of over 40 m s^{-1} at 10 m above the sea surface just before its reentry to MAB (Figure 1b). Strong cyclonic winds blew across the entire MAB and the adjacent deep ocean (Figure 1c). MSW decreased to about 32 m/s when the center of the storm reached the New England shelf. A network of High-frequency (HF) radars recorded the surface currents generated by Arthur as it propagated northeastward from the Outer Banks of North Carolina to the New England Shelf. A Slocum glider was deployed off the New Jersey Coast prior to the arrival of Hurricane Arthur. It obtained vertical profiles of temperature, salinity, and currents in the water column during Arthur's passage over the MAB. These observations, along with hindcast simulations from a three-dimensional numerical model, can be pieced together to produce a detailed three-dimensional view of the MAB's response to Hurricane Arthur. The numerical model, once validated against the observations, can be used to probe mechanisms driving the spatial and temporal variabilities of the NICs on the shelf.

This paper is organized as follows. Section 2 reports observations of the NICs generated by Hurricane Arthur. Section 3 describes the numerical model. Section 4 shows the model results and the analysis of the near-inertial wave dynamics. Finally, conclusions are made in section 5.

2. Observations of Near-Inertial Currents

2.1. Surface Currents From High-Frequency Radars

HF radar surface currents were mapped using a network of CODAR SeaSonde stations distributed across the MAB. HF radar measures the radial component of ocean surface currents using the Doppler shift of backscattered radio frequencies from surface waves (Barrick, 1971a, 1971b; Teague, 1971). Total surface current vectors are determined by combining overlapping radials using an optimal interpolation method to produce hourly surface current maps. Kohut et al. (2012) conducted a detailed analysis on the uncertainty of HF radar velocity measurements. They compared the HF radar velocities against the velocities measured by Acoustic Doppler Current Profilers (ADCPs). The root-mean-square differences between the two measurement techniques were typically below 10 cm/s, on the same order of magnitude as the differences between

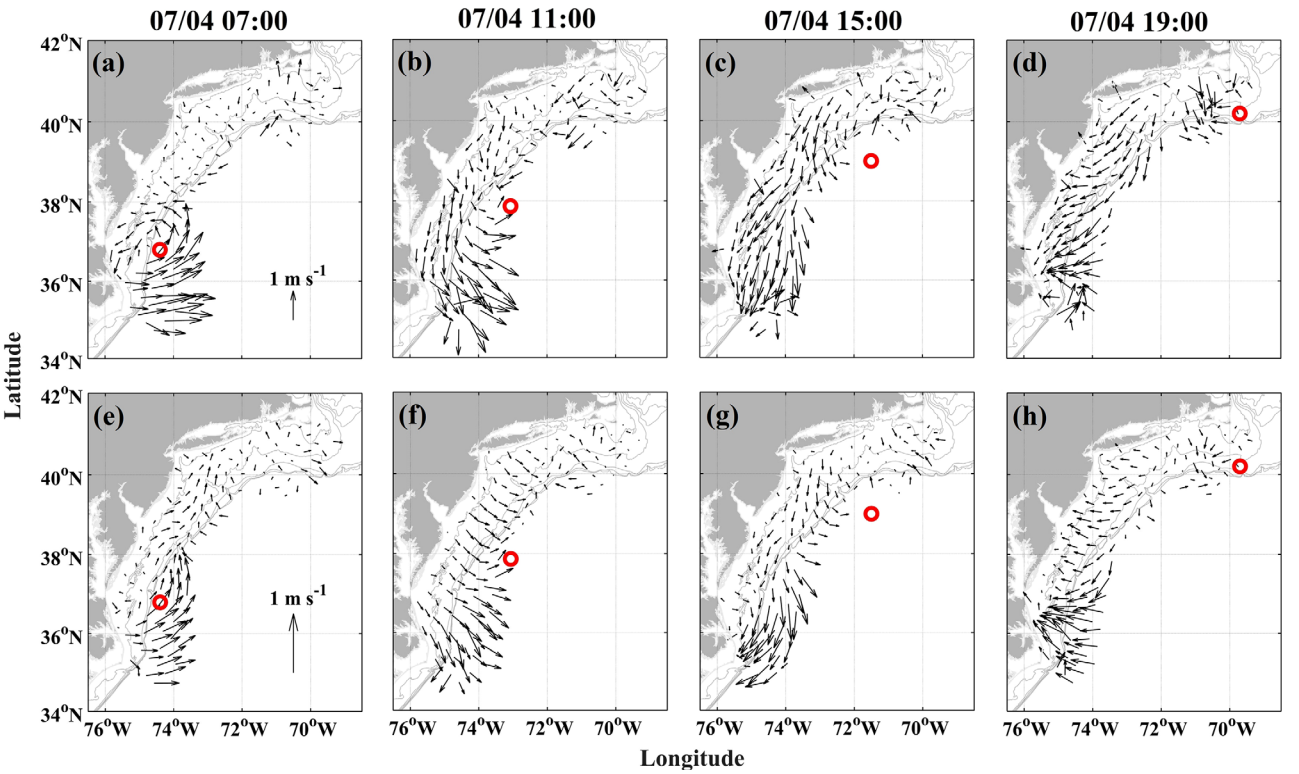

Figure 2. Surface subtidal currents observed by HF radar at (a) 07:00 LST 4 July, (b) 11:00 LST 4 July, (c) 15:00 LST 4 July, and (d) 19:00 LST 4 July. (e)–(h) Surface NICs at the same times as Figures 2a–2d. The red circle marks the storm center in each snapshot.

the spatially separated ADCPs themselves. The measurement discrepancies were attributed to differences in the spatial sampling resolution (~6 km resolution in the 5 MHz HF radar versus point measurements in ADCP) as well as possible mismatches in the measurement depth for the ocean surface layer (~2.4 m for HF radar versus the upper bin width of the ADCP). The HF radar network used in this study sampled across the continental shelf from the shore out to the shelf-break in ideal wave conditions (Roarty et al., 2010). This system is operated by the Mid-Atlantic Regional Association Coastal Ocean Observing System (MARACOOS, https://maracoos.org/) and was recently repaired and hardened for tropical cyclone impacts based on damages sustained during Hurricane Sandy.

The HF radars produced a sequence of maps of the surface currents as Hurricane Arthur made its way northeastward from Outer Banks of North Carolina to New England Shelf (Figures 2a–2d). To focus on the currents generated by the storm, harmonic analysis was applied to extract and remove tidal signals from the HF radar data. At 07:00 LST 4 July (Figure 2a), Arthur's center was off the mouth of Chesapeake Bay. A cyclonic current pattern developed in the southern MAB, mirroring the wind stress curl generated by the storm (Figure 6a). The currents were much stronger (over 1 m s^{-1}) on the right-hand side of the storm track than those on the left-hand side (~0.5 m s^{-1}). Farther north, the surface currents were weak (~0.2 m s^{-1}) and mostly directed onshore, likely driven by the easterly winds in the front quadrants of the storm. As Arthur moved northward and further offshore (Figure 2b), southward currents occupied the southern and middle parts of the MAB shelf (New Jersey Coast to Outer Banks of North Carolina) while the currents off

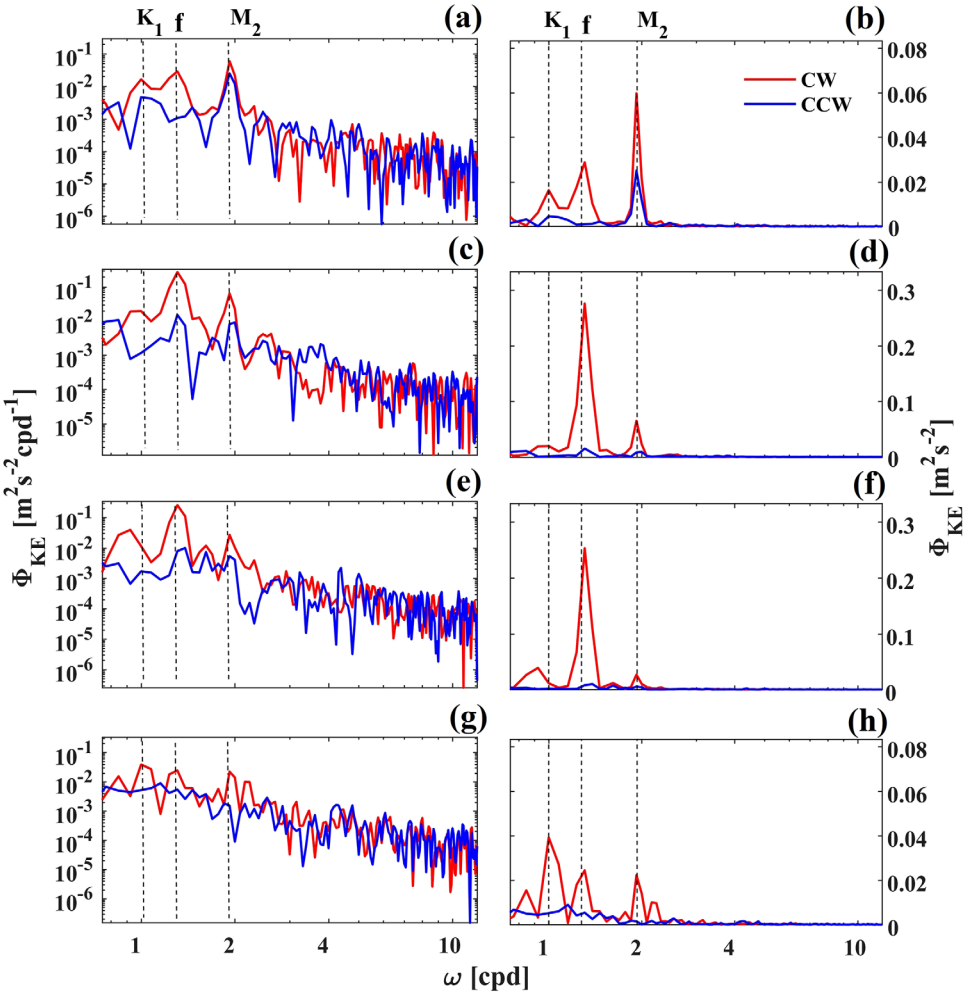

Figure 3. (a, c, e, g) Rotary spectra and (b, d, f, h) variance-preserving spectra for the surface currents at three locations in a northern MAB section and one location in southern MAB (their locations marked by large magenta symbols in Figure 1c). The spectra are calculated from the HF radar time series between 2 and 12 July.

Cape Hatteras were offshore. At 15:00 LST 4 July when the storm center was located off the New Jersey Coast (Figure 2c), the southward currents spread across the entire MAB shelf. Noticeably, the surface currents in the middle part of MAB (off New Jersey Coast and Long Island Coast) increased from ~0.2 to ~0.7 m s^{-1}, while the currents on the southern MAB decreased slightly. At 19:00 LST 4 July (Figure 2d), Arthur was located over the shelf-break south of Cape Cod. Cyclonic currents developed there, with southward currents on the rest of the MAB shelf.

NICs were a major component of the storm-driven currents and were extracted from the detided currents using a sixth-order bandpass Butterworth filter set at (0.8–1.2) *f* (local inertial frequency). HF radar data with less than 90% temporal coverage were excluded from the analysis, and other smaller data gaps were patched using linear interpolation. At 07:00 LST 4 July, the surface NICs showed strong cyclonic currents (>0.5 m s^{-1}) on the right side of the storm's center but weak currents (<0.2 m s^{-1}) on the inner shelf (Figure 2e). As Arthur continued its path northward and off to the deep ocean, the HF radar could only provide a partial view of the surface currents up to the shelf-break (Figures 2f–2h). Nonetheless, NICs, rotating clockwise in time with a velocity magnitude of 0.1–0.3 m s^{-1}, were observed throughout the MAB shelf. At 19:00 LST 4 July, strongest NICs were still seen in southern MAB even though the storm's center had already moved to the New England Shelf (Figure 2h).

When a hurricane moves over the deep ocean, the dominant oceanic response is the NICs (Price, 1983; Price et al., 1994; Sanford et al., 2007, 2011). When a hurricane moves over the continental shelf, however, other types of currents could be generated (Glenn et al., 2016). To discern the role of NICs on the shelf, we calculated the rotary spectra using the HF radar total velocity time series between 2 and 12 July at four locations: an inshore location (~30 m isobath, near the glider track), a midshore location (~50 m isobath, midpoint between the glider and buoy) and an offshore location (~80 m isobath, Buoy 44066) along a cross-shelf section off New Jersey Coast; a location off the Virginia Coast (Figure 3). At the inshore location with strong semidiurnal tides, the NICs only had less than one-half of the M_2 tidal energy, although it was still higher than K_1 tide (Figures 3a and 3b). At the midshore and offshore locations (Figures 3c–3f), however, NICs had much higher energy content than the tidal components and dominated the energy spectrum. At the southern station off the Outer Banks, the spectrum had a peak at 1 d^{-1} frequency, but diurnal tides are weak there (Lentz et al., 2001). The peak probably represented the wind-driven longshore currents in this region (see Figures 2a–2d). Figure 2 clearly shows large differences between the total subtidal currents and the NICs in the southern MAB (compare the top and bottom plots). Overall, NICs were a major component of the shelf currents on the MAB during the passage of Hurricane Arthur.

2.2. Glider Observations

Autonomous underwater gliders have become reliable storm sampling platforms (Glenn et al., 2016; Miles et al., 2013, 2015, 2017) capable of obtaining high vertical resolution data at ~2 Hz with fall speeds on the order of 0.1 m s^{-1}. The glider uses a combination of adjustable buoyancy and a set pitch angle to achieve forward motion at nearly 20 km d^{-1}. The data used in this study were collected by a Slocum glider, RU30, operated by Rutgers University. This system was equipped with a suite of oceanographic sensors, including (1) a Seabird Scientific pumped conductivity-temperature-depth (CTD) sensor, (2) a Wetlabs Inc. eco-triplet measuring chlorophyll fluorescence (chl), colored dissolved organic matter (CDOM), and optical backscatter at 700 nm wavelength (bb700), (3) an Aandera oxygen optode in the aft section measuring oxygen concentration and saturation, and (4) an externally mounted upward looking Nortek 1 MHz Aquadopp current profiler. The Aquadopp was designed to collect data on downcasts at a nominal pitch angle of 26.5°, which oriented the three-beam transducers vertically upward. The Aquadopp was configured to collect data at 1 Hz with 10 bins. Compass calibration was performed prior to deployment, including a 24 point check with a hand compass to provide postdeployment corrections for known elliptical biases exaggerated in the eastward and westward directions. Absolute current velocities were calculated following standard LADCP procedures that had been adapted to use on shallow Slocum glider platforms (Miles et al., 2017).

The glider was deployed off the New Jersey Coast prior to the arrival of Hurricane Arthur. The glider moved around (73.6°W, 39.7°N) between 4 and 8 July and trespassed an area no larger than 60 km^2 (Figure 4a). Figure 4b showed the time series of the wind speed vector measured at a buoy further offshore (Buoy 44066 of the National Data Buoy Center). The winds there rotated counter-clockwise during Arthur's passage, switching from northeasterly on 4 July to southwesterly on 7 July. The peak wind speed reached over 20 m s^{-1} on 4 July. The glider observed strong stratification on the shelf, with a sharp thermocline separating the warm

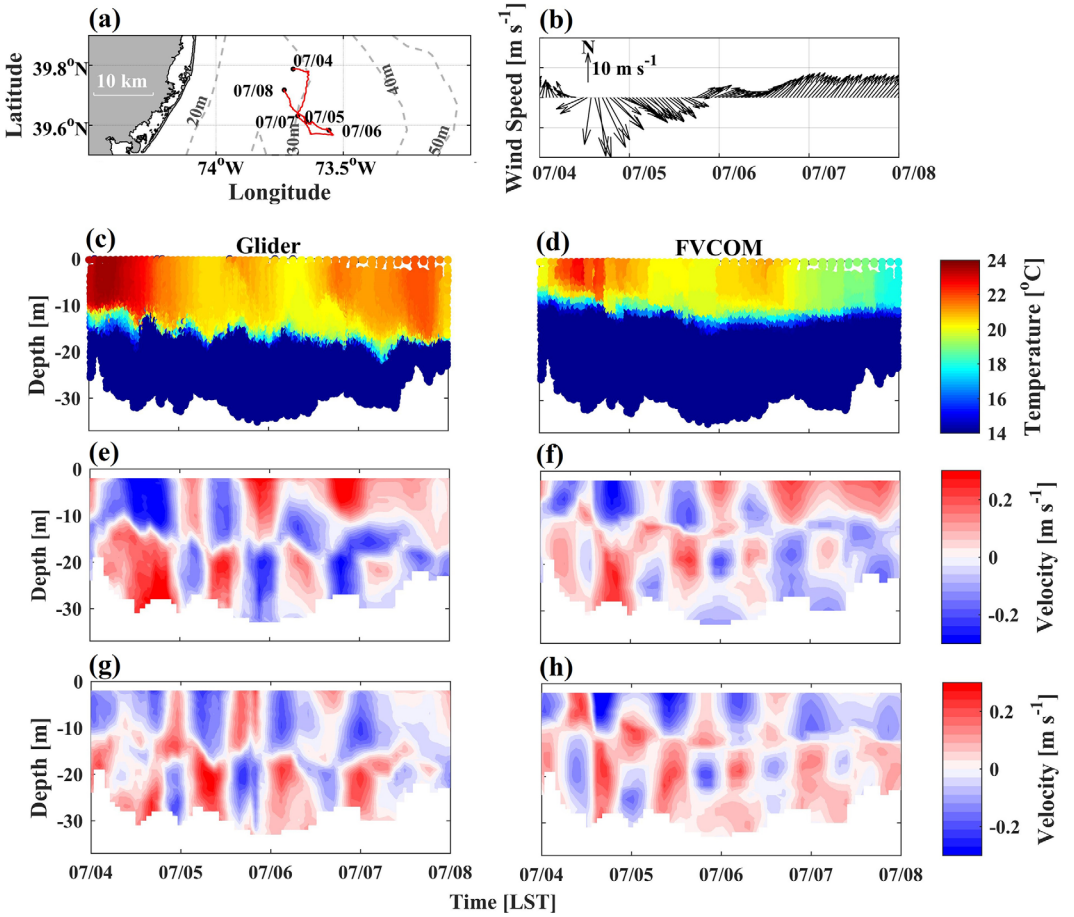

Figure 4. (a) Zoomed-in view of the glider track (red line). (b) Time series of the wind speed vector measured at the Buoy 44066. Time-depth distributions of (c, d) temperature, (e, f) zonal, and (g, h) meridional baroclinic velocity components obtained (left column) from the glider measurements and (right column) from the FVCOM model.

surface water from the cold bottom water as shown in Figure 4c (the density field displays essentially the same vertical structure). On the MAB, a band of cold bottom water occupies the shelf from spring to fall (Castelao et al., 2010; Houghton et al., 1982; Lentz, 2017). Prior to the arrival of Arthur, temperature in the surface layer was nearly uniform and at 24°C whereas temperature in the bottom Cold Pool was around 11°C. These compare with the long-term averaged surface layer temperature of ~22°C and bottom water temperature of ~11°C in July (Castelao et al., 2010; Fleming, 2016), indicating that the stratification on the MAB prior to Arthur's arrival was slightly stronger than the average. In addition, the thermocline depth was at ~13 m, shallower than the ~17 m found in the monthly climatology for July. Wind-induced mixing caused the surface mixed layer to deepen from ~13 to ~18 m. In the mean time, temperature in the surface mixed layer decreased from 24 to 20°C. After Arthur's departure surface layer, temperature bounced back to 22°C.

The glider made repeated profiling of currents in the water column over the 4 day deployment period. After the depth-averaged current was removed, both the zonal and meridional velocities displayed a mode-1 baroclinic structure, reminiscent of the mode-1 near-inertial waves as observed by MacKinnon and Gregg (2005) and Shearman (2005) on the New England shelf (Figures 4e and 4g). These baroclinic currents oscillated at a period of about 18 h and were essentially the NICs. The surface and bottom NICs had a similar velocity magnitude (~0.2 m s^{-1}).

3. Model Description

To interpret the observed spatial and temporal variabilities of NICs, a three-dimensional hydrodynamic model based on the unstructured-grid Finite Volume Coastal Ocean Model (FVCOM) (Chen et al., 2003) was

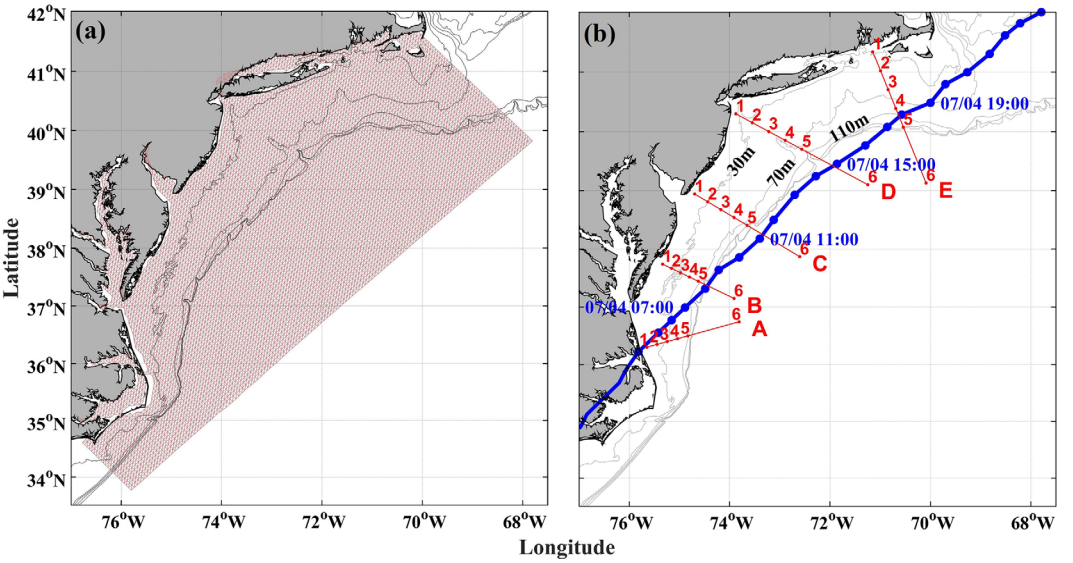

Figure 5. (a) FVCOM model grids over MAB. (b) Five representative cross-shelf sections (marked as A–E, red lines) used to investigate the spatial variability of NICs over MAB. In each section, six points (numbered 1–6) are selected for detailed analysis in Figures 7 and 11. The blue line with solid dots marks the storm's track and the bathymetry is shown as gray contour lines.

configured for the MAB and adjacent estuaries including Chesapeake Bay, Delaware Bay, and Long Island Sound (Figure 5a). The eastern boundary is placed about 300 km from the coast while the southern and northern boundaries are roughly perpendicular to the coast, located at 34°N and 42°N, respectively. The model domain covers the entire MAB shelf from Cape Hatteras, North Carolina, to Cape Cod, Massachusetts with a horizontal resolution of ~5 km. The bathymetry data were extracted from the 1 arc min ETOPO1 Global Relief Model (Amante & Eakins, 2009). In the vertical direction, a hybrid coordinate system is used. The water column is evenly divided into 30 levels when water depth is less than 150 m. When water depth exceeds 150 m, however, both the surface mixed layer and bottom boundary layer are discretized into 5 layers with a thickness of 5 m in each layer while the rest of the water column is evenly divided into 20 levels. The horizontal eddy viscosity and diffusivity are set to 0.1 and 1 $m^2\ s^{-1}$, respectively. The vertical eddy viscosity and diffusivity are computed using the $k-\varepsilon$ turbulence closure scheme incorporated into the General Ocean Turbulent Model (Burchard, 2002; Warner et al., 2005), and the background diffusivity and viscosity are 10^{-5} and $5\times10^{-6}\ m^2\ s^{-1}$, respectively. A quadratic stress is applied at the sea bed, assuming that the bottom boundary layer is logarithmic with a roughness height of 2 cm (Churchill et al., 1994), same as that used in Experimental System for Predicting Shelf and Slope Optics (ESPreSSO, http://www.myroms.org/espresso/). A barotropic version of this model was used to study tides and storm surge in Lee et al. (2017) and Zhang et al. (2017).

For the baroclinic version used in this study, the FVCOM model is initialized on 1 January 2014 with fine-resolution predictions of temperature, salinity, and sea level from the ESPreSSO. At the offshore open boundary, the tidal variation of sea level is prescribed using five tidal constitutes (M_2, S_2, N_2, K_1, and O_1) from the Oregon State University global tidal model TPXO 7.1 (Egbert & Erofeeva, 2002). In order to simulate the effects of the Gulf Stream and large-scale currents on the MAB shelf, the regional FVCOM model is nested into Hybrid Coordinate Ocean Model and Navy Coupled Ocean Data Assimilation systems (HYCOM-NCODA, http://hycom.org) using one-way nesting, for which the inner model receives its boundary values from the outer model at the inner model open boundaries. This is consistent with the configuration of the initial condition since ESPreSSO is also forced by HYCOM-NCODA at its open boundaries. The daily data of sea surface height, salinity, temperature, and current velocities are extracted from the HYCOM-NCODA database and interpolated to the open boundary nodes of the regional FVCOM model. They provide the subtidal component of the open boundary conditions while the tidal component is obtained by running the regional model with tidal forcing only. The two components are then added together to prescribe the open boundary conditions for the regional FVCOM model. The surface momentum and heat fluxes are prescribed

using hourly outputs from the Weather Research and Forecasting (WRF) model that was developed to predict Hurricane Arthur between 2 and 6 July (Zhang et al., 2017), and using the outputs from the North American Regional Reanalysis (NARR, https://www.esrl.noaa.gov/psd/data/gridded/data.narr.html) at 3 h intervals during other times of the model integration. The freshwater flows from Susquehanna River, Delaware River, Hudson River, and other small tributaries are prescribed according to measurements at the U.S. Geological Survey water gauge stations.

4. Model Results

4.1. Spatial and Temporal Variabilities of NICs

Since its range was limited to the shelf-break, HF radars only provided a partial view of the surface currents generated by Hurricane Arthur. On the other hand, the regional FVCOM model provided a complete view of the current field (Figure 6). To help understand the storm-driven currents, surface winds from the WRF model are shown in Figures 6a–6d. The FVCOM model did a good job in capturing the dominant current patterns observed during Arthur's passage over the MAB shelf (compare Figures 2a–2d and 6e–6h): cyclonic currents around the storm's center at 07:00 LST 4 July and strong southward currents over the entire shelf over the next 12 h. The model also showed that strong cyclonic currents continued to develop underneath the storm's center as Arthur moved northeastward, and tracked the patterns of wind stress curl produced by the storm (Figures 6a–6d). The currents had strong left-to-right asymmetry across the storm's track: the

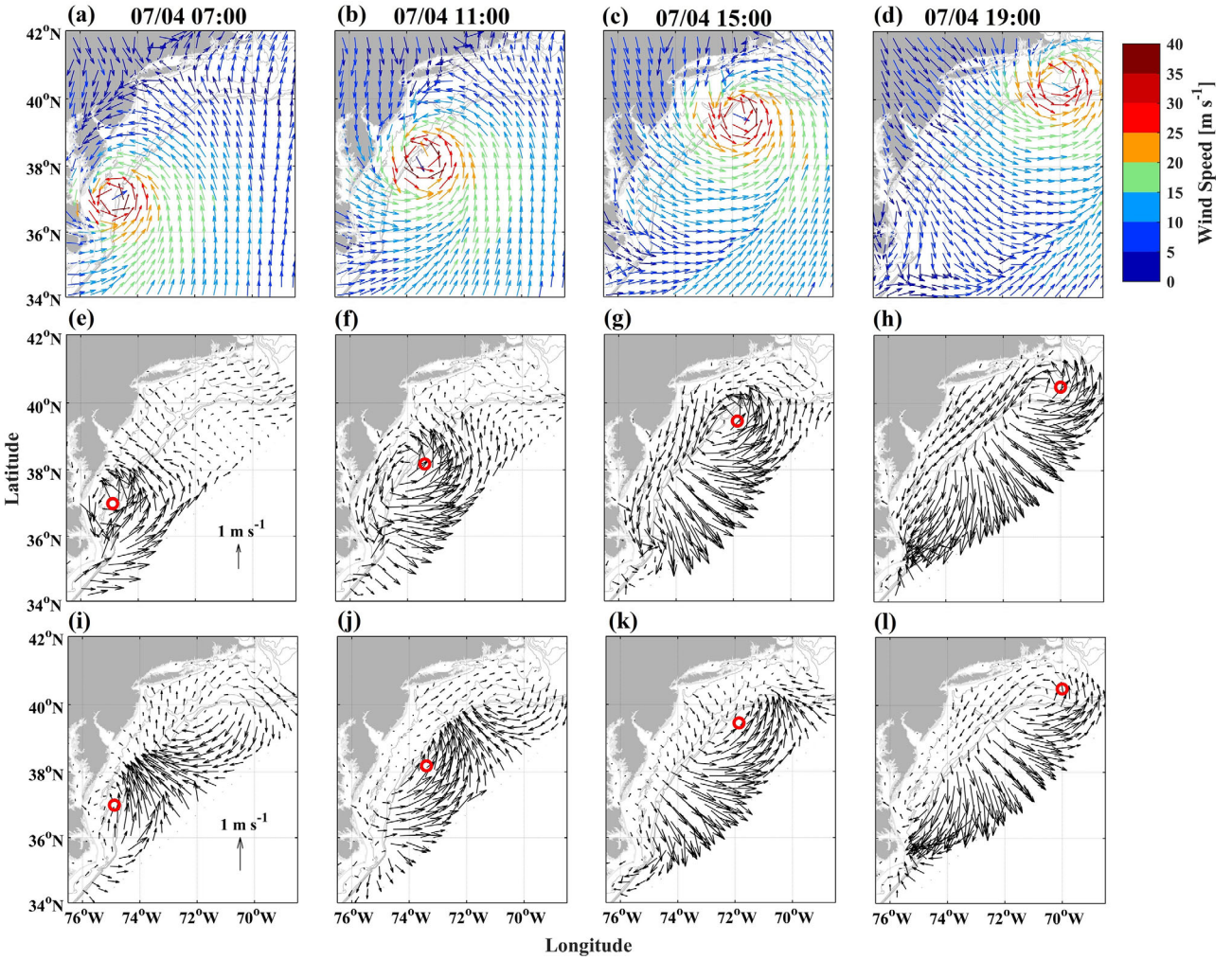

Figure 6. WRF-predicted wind speed vectors at 10 m height at (a) 07:00 LST, (b) 11:00 LST, (c) 15:00 LST, and (d) 19:00 LST 4 July. FVCOM-predicted (e)–(h) surface subtidal currents and (i)–(l) surface NICs at the same times as (a)–(d).

currents on the right side of the storm's center were over twice stronger than those on the left side. The currents in the near-inertial frequency range ($0.8 - 1.2f$), namely NICs, also displayed the strong left-to-right asymmetry (Figures 6i–6l). However, NICs did not show strong cyclonic currents underneath the storm's center. The NICs at any particular location were initially generated by the strong winds in the right front quadrant and then rotated clockwise due to the action of the Coriolis force. One can clearly see the stronger NICs in the deep ocean to the right of the shelf-break (Figures 6i–6l). On the MAB shelf, the NICs were considerably weaker.

The above snapshots describe the spatial variations of NICs at four different times during Arthur's transit over MAB. To further investigate the temporal evolution of NICs, we plot 14 day time series of NICs at a number of virtual sampling stations (Figure 7). Five cross-shelf sections are selected to represent the southern, middle, and northern regions of MAB (Figure 5b): Section A extends offshore from the Outer Banks of North Carolina where Arthur re-entered the North Atlantic; Section B extends offshore from the Delmarva Peninsula (midpoint between the mouths of Chesapeake and Delaware Bays); Section C is placed off the southern New Jersey Coast (north of Delaware Bay); Section D is located in the Hudson Shelf Valley which has the deepest bathymetry on the MAB; and Section E is positioned east of Long Island Sound to cover the New England Shelf. Along each cross-shelf section, five stations are evenly spaced out on the shelf and one station is located offshore of the shelf-break. The time series of NICs were extracted from both the HF radar observations and the FVCOM model outputs using harmonic analysis and bandpass filter described in section 2. Velocities in the zonal and meridional directions were rotated to the cross-shelf and along-shelf directions. Since the cross-shelf and along-channel velocities showed similar temporal variabilities and were of similar magnitude, our analysis focuses on the cross-shelf velocity in Figure 7.

At each cross-shelf section, the NICs on the shelf were about one-fourth to one-third of those (about 1.2 m s^{-1}) in the deep ocean and decreased from the shelf-break to the inner shelf (Figure 7). The NICs had a peak magnitude of 0.3 m s^{-1} in southern MAB (Section A) but decreased to 0.2 m s^{-1} in the middle part of MAB (Sections B and C). They rebounded to 0.3 m s^{-1} in northern MAB (Sections D and E), even though the maximum surface winds decreased from ~40 m s^{-1} in the southern MAB to ~30 m s^{-1} in the northern MAB (Figure 1b). One also notices interesting differences in the temporal evolution of the NICs between the

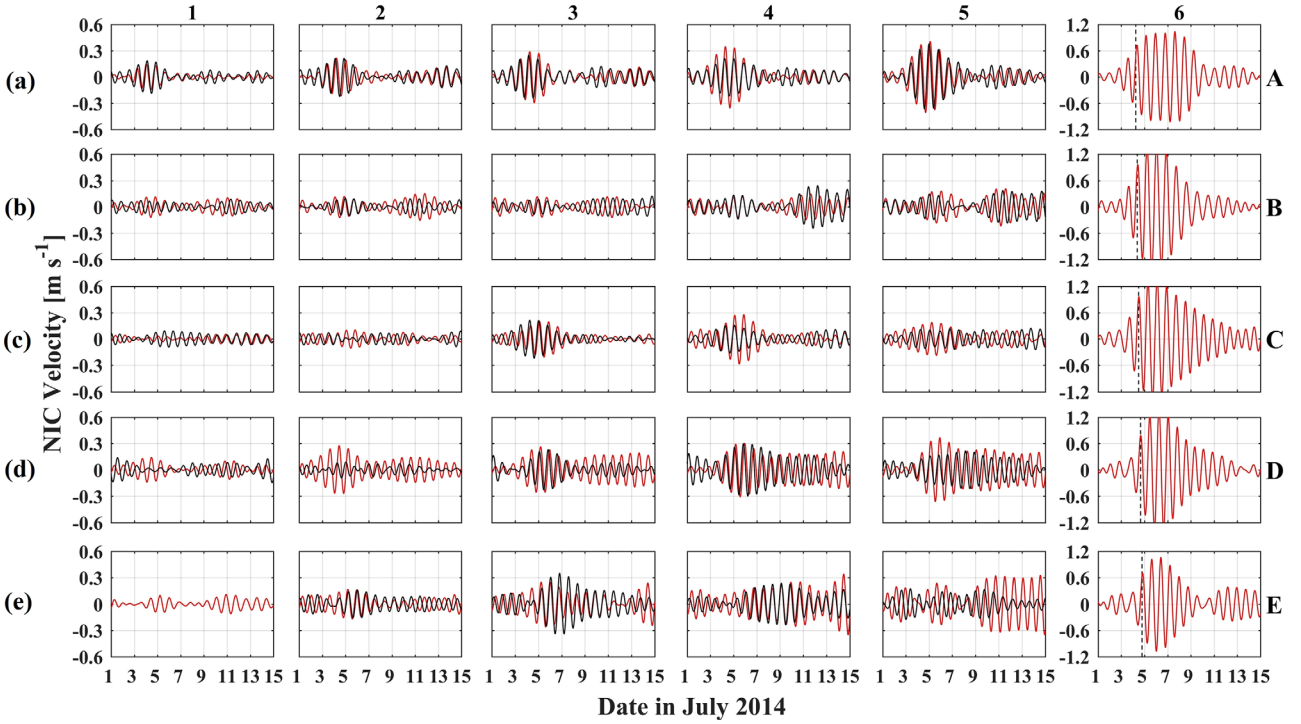

Figure 7. Time series of the cross-shelf component of the surface NICs at six virtual sampling stations (numbered 1–6) along the cross-shelf Sections A–E over MAB: HF radar observations (black) and FVCOM model result (red). The dashed black lines in column 6 indicate the times when Arthur was closest to each section.

southern and northern parts of MAB. The NICs in the southern MAB shelf attenuated quickly and lasted for 3–4 days (Figure 7a). In contrast, the NICs in the northern MAB shelf persisted for ~10 days. They are in general good agreements on the spatial and temporal variabilities of NICs between the model predictions and HF radar observations. Averaged over all stations, the correlation coefficient between the predicted and observed NICs is 0.48 and the root-mean-square error is 0.09 m/s. One exception is E5 where the observed NICs displayed a rapid decay after 11 July but the predicted NICs persisted. A possible cause for the discrepancy is that E5 was the farthest station from the coast (at the shelf-break) and the HF radar measurements there may be inaccurate. Observations at nearby stations such as E4, D5, and D4 showed sustained NICs consistent with the model results. The observed and predicted NICs show phase differences at some locations such as C5 and D5. Given their close proximity to the storm track, a small difference between the predicted and observed tracks (about 50 km, see Figure 1c and Zhang et al., 2017) could cause these phase differences.

4.2. Energy Budget Analysis

As a step toward understanding the spatial variability of the NICs generated by Hurricane Arthur, we mapped out the spatial distribution of the depth-integrated kinetic energy (*KE*) of the near-inertial waves and compared it with the wind energy input to the near-inertial frequency band. The depth-integrated *KE* is given by

$$KE = \int_{-H}^{0} \frac{1}{2}\rho|\vec{U}'|^2 dz \tag{1}$$

where H is the water depth, ρ is the density, and $\vec{U}'$ is the horizontal velocity vector in the near-inertial frequency band. *KE* is averaged over the 10 day period (2–12 July) when the NICs were affected by Arthur. *KE* was much larger in the deep ocean than on the shelf, and was low near the coast but increased in the offshore direction (Figure 8a). There was a band of relatively high *KE* in the midshelf region between the Nantucket Shoals and Atlantic City, New Jersey. In contrast, *KE* was considerably lower in the midpart of MAB (Sections B and C) between Ocean City, Maryland and Atlantic City, New Jersey (see Figure 1a for a map of these geographic locations).

Much of the *KE* differences between the MAB shelf and the deep ocean may be explained by the asymmetry in the wind energy input to the near-inertial waves,

$$W_{\tau s} = \vec{\tau}_s \cdot \vec{U}'_s \tag{2}$$

where $\vec{\tau}_s$ is the surface wind stress vector and $\vec{U}'_s$ is the surface NICs velocity vector, following the approach of D'Asaro (1985). $W_{\tau s}$ was averaged over the same 10 day period as for *KE*. The wind energy input showed strong left-to-right asymmetry with respect to the storm's track (Figure 8b). Therefore, a large part of the *KE*

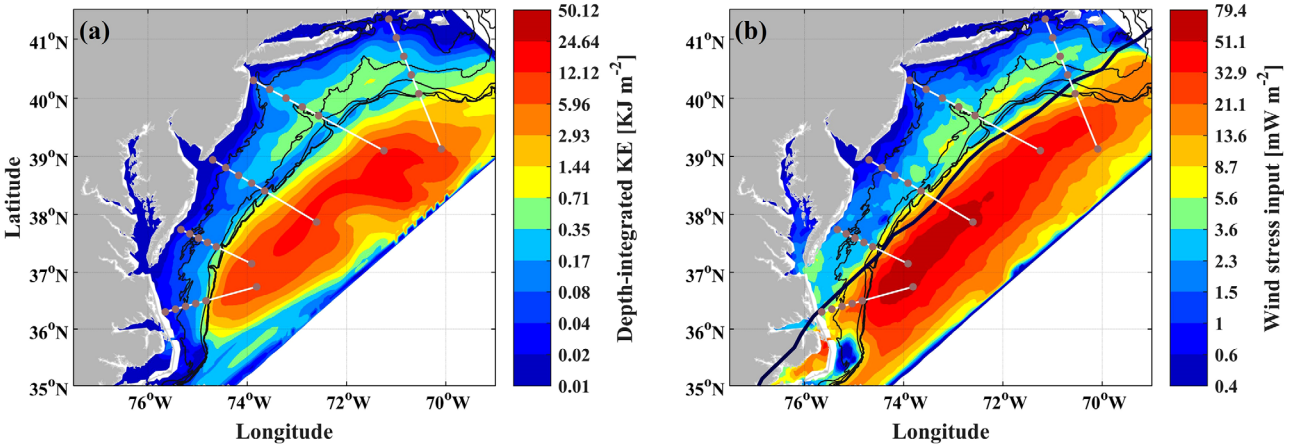

Figure 8. (a) Depth-integrated kinetic energy of the near-inertial waves and (b) wind energy input into the near-inertial waves. Both are averaged between 2 and 12 July. The five cross-shelf sections as well as the virtual sampling points used in Figure 7 are shown. The thick black line in Figure 8b represents the predicted storm's track. Color-bars are in logarithmic scale.

differences between the shelf and the deep ocean was simply due to the left-to-right asymmetry in $W_{\tau s}$. On the MAB shelf itself, the band of relatively high *KE* in the midshelf region between the Nantucket Shoals and Atlantic City was also associated with higher wind energy input into the near-inertial waves. However, there was no one-to-one correspondence between *KE* and $W_{\tau s}$. In the southern MAB (including the cross-shelf Section A), the time-averaged *KE* was low but $W_{\tau s}$ was high there (compare Figures 8a and 8b).

Further insights into the wind generation of NICs can be obtained by comparing the time series of the wind energy input at different locations. At station D6 in the deep ocean, which lay on the right side of the storm's track, the wind stress vector rotated clockwise and remained nearly parallel with the clockwise-rotating NICs (Figures 9a and 9b). This resulted in a large flux (a maximum of ~3 W m^{-2}) of wind energy to the NICs (Figure 9c) and rapid increase of surface NICs from 0.3 m s^{-1} on early 4 July to 1.2 m s^{-1} on 5 July (Figure 9b). At the shelf station D5 on the left side of the track, the wind stress was 50% smaller and rotated counter-clockwise (Figure 9d) while the NICs rotated clockwise (Figure 9e). Consequently, the coupling between the wind stress and inertial currents was much less efficient and produced an energy flux (a maximum of ~0.3 W m^{-2}) that was only 10% of that at station D6 (Figure 9f). The surface NICs at D5 only reached about 0.2–0.3 m s^{-1}, approximately one-fourth of the NICs speed at D6. At the shelf station B5 further south, which was located closer to the storm's center, the magnitude of the wind stress was larger than that at D5 (compare Figures 9g and 9d). Initially the northwestward wind stress coincided with the northwestward NICs, producing a pulse of wind energy to NICs. Later on, however, the wind direction shifted by 180° and became southwestward while the NICs were still directed in the northwest directions (Figures 9g–9h). This resulted in negative wind work because the wind stress vector and the NICs vector varied out of the phase (Figure 9i). When integrated over time, the net wind energy input to NICs was much lower at B5. This explains the low *KE* level in the middle part of MAB (between Ocean City, Maryland and Atlantic City, New Jersey).

An understanding of the discrepancy between *KE* and $W_{\tau s}$ in southern MAB requires us to examine other terms in the energy budget for the near-inertial waves (e.g., Chant, 2001; Zhai et al., 2009):

$$\frac{\partial KE}{\partial t} = W_{\tau s} - W_{\tau b} - \varepsilon - \int_{-H}^{0} PEC \; dz - \int_{-H}^{0} \nabla \cdot KE_{adv} \; dz - \int_{-H}^{0} \nabla \cdot F \; dz + others \tag{3}$$

where $W_{\tau b}$ is the bottom friction work, ε is the depth-integrated dissipation of *KE* associated with vertical viscosity, *PEC* is the conversion rate of *KE* into potential energy of near-inertial waves, KE_{adv} is the advection of *KE*, *F* is the near-inertial wave energy flux, and *others* include nonlinear energy transfer to other frequency

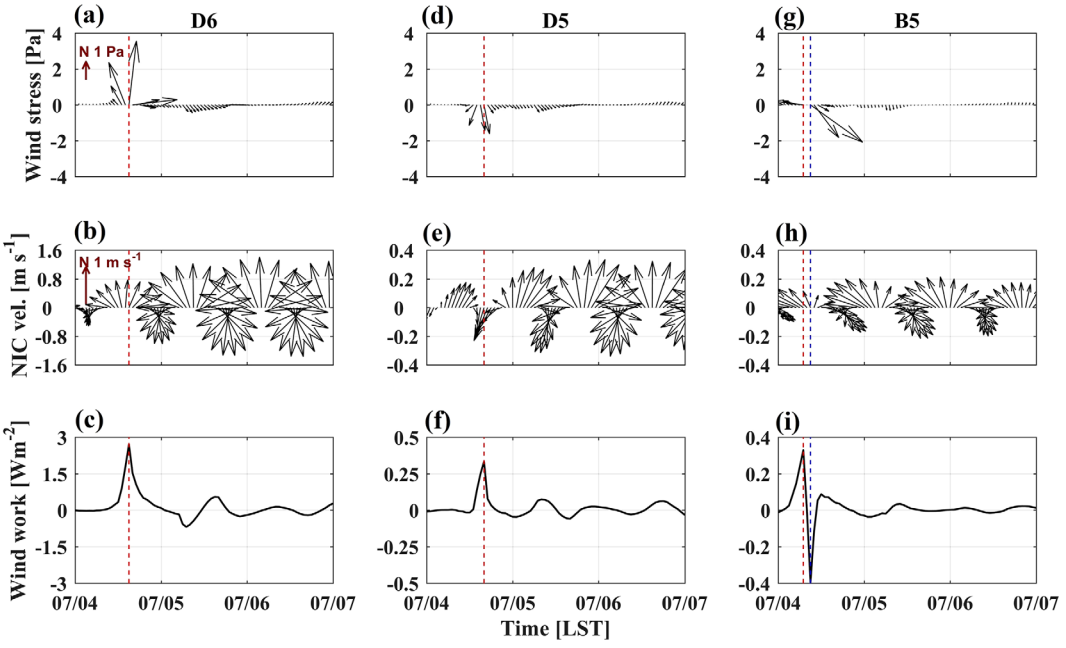

Figure 9. (a, d, g) Surface wind stress, (b, e, h) surface NICs, and (c, f, i) wind energy input obtained from the WRF-FVCOM models: D6 (left column), D5 (middle column), and B5 (right column). In the right column, the red-dashed lines indicate the time of peak positive wind work, and the blue-dashed lines indicate the time for peak negative wind work.

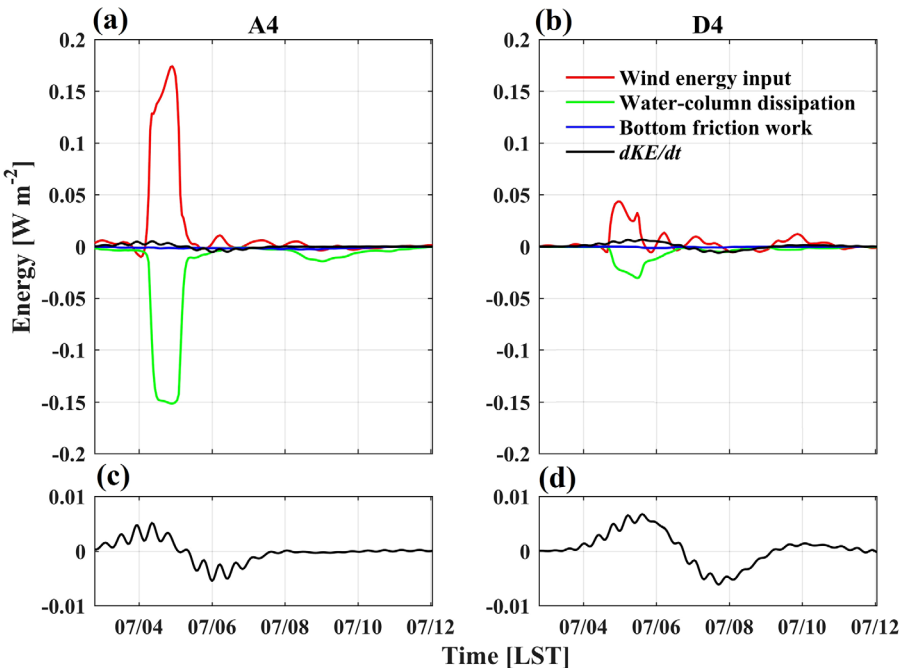

Figure 10. Wind energy input (red), the depth-integrated water-column dissipation of NIC kinetic energy (ε, green), bottom friction work (blue), and depth-integrated *dKE/dt* averaged over the inertial period for (a) A4 and (b) D4. Zoomed-in view of *dKE/dt* for (c) A4 and (d) D4.

bands and the depth-integrated dissipation of *KE* associated with horizontal viscosity. The bottom friction work can be written as

$$W_{\tau b} = \vec{\tau_b} \cdot \vec{U_b'} \tag{4}$$

where $\vec{\tau_b}$ is the bottom stress and $\vec{U_b'}$ is the bottom NICs velocity. The depth-integrated dissipation of *KE* due to vertical viscosity is calculated by

$$\varepsilon = \int_{-H}^{0} \rho K_v \left(\frac{\partial^2 u'}{\partial z^2} + \frac{\partial^2 v'}{\partial z^2} \right) \tag{5}$$

where K_v is the vertical eddy viscosity and u' and v' are the zonal and meridional NICs velocity components, respectively.

We compared the energy budget balance at two locations on the MAB shelf: station A4 where NICs were strong initially but damped out quickly (Figure 7a) such that the time-averaged *KE* was low (Figure 8a); station D4 where NICs were strong and persisted for ~10 days (Figures 7d and 8a). Figure 10 shows that the primary balance in the kinetic energy budget was between the wind energy input and energy dissipation. At station A4 in the southern MAB, the wind energy input was high due to its closeness to the storm's center and strong winds. It was counter-balanced by strong energy dissipation. In contrast, both the wind energy input and dissipation were much smaller at D4 in the northern MAB. Therefore, in the southern MAB, the strong energy dissipation constrained the growth of NICs energy even though the wind work was larger there. The frictional dissipation in the bottom log layer was less than 10% of ε. The energy dissipation ramped up quickly at the southern station A4 to balance the wind work such that *dKE/dt* switched from positive sign to negative sign in early 5 July (Figure 10c). This explains the rapid damping of NICs seen in Figure 7 (first row). On the other hand, there was a delay for the dissipation to catch up with the wind input at the northern station D4 such that $dKE/dt > 0$ until 7 July (Figure 10d). Hence, the NICs at D4 persisted for up to 10 days.

4.3. Vertical Modal Structure

The glider deployed in the inner shelf off the New Jersey Coast observed two-layer baroclinic currents during the passage of Hurricane Arthur (Figures 4e and 4g). The FVCOM model reproduced this two-layer

current structure that oscillated at the local inertial frequency (∼19 h) (Figures 4f and 4h). Both the amplitude and phase of the observed current fluctuations were reasonably simulated. The model also captured the observed two-layer stratification, with the warm surface water separated from the cold pool water by a sharp thermocline (compare Figures 4c and 4d). However, there were model-data discrepancies. The predicted surface mixed-layer depth prior to Arthur's arrival was about ∼8 m, and was shallower than the observed depth of ∼13 m. Turbulent closure schemes (such as the $k-\varepsilon$ model used in this study) do not fully account for the mixing processes in the surface mixed layer such as Langmuir circulation and breaking waves, and tend to underpredict the mixed-layer depth (e.g., Belcher et al., 2012; Burchard & Bolding, 2001; Mellor, 2001). Our model was initialized using the outputs from ESPreSSO. While data assimilation in ESPreSSO should significantly reduce the model-data misfit, it is possible that part of our model discrepancies with the observations may have originated from possible misfit in the initial condition. Nevertheless, the model and glider showed similar rates of the mixed-layer deepening and temperature decrease due to the storm-induced entrainment: the mixed layer deepened by 6 m in the model and by 5 m in the glider observations.

To investigate the vertical structure of NICs over the entire MAB shelf, we plot the time-depth distribution of NICs at the stations spaced along the five cross-shelf sections (Figure 11) as indicated in Figure 5b. The pycnocline, defined to be the location of maximum density gradient, is added, in order to highlight the connection between the stratification and vertical modal structure of the NICs. A comparison of the current structure between the deep ocean and shelf stations showed a marked difference. Strong NICs in the deep ocean penetrated down to ∼100 m and exhibited a vertical profile typical of the NICs observed in deep

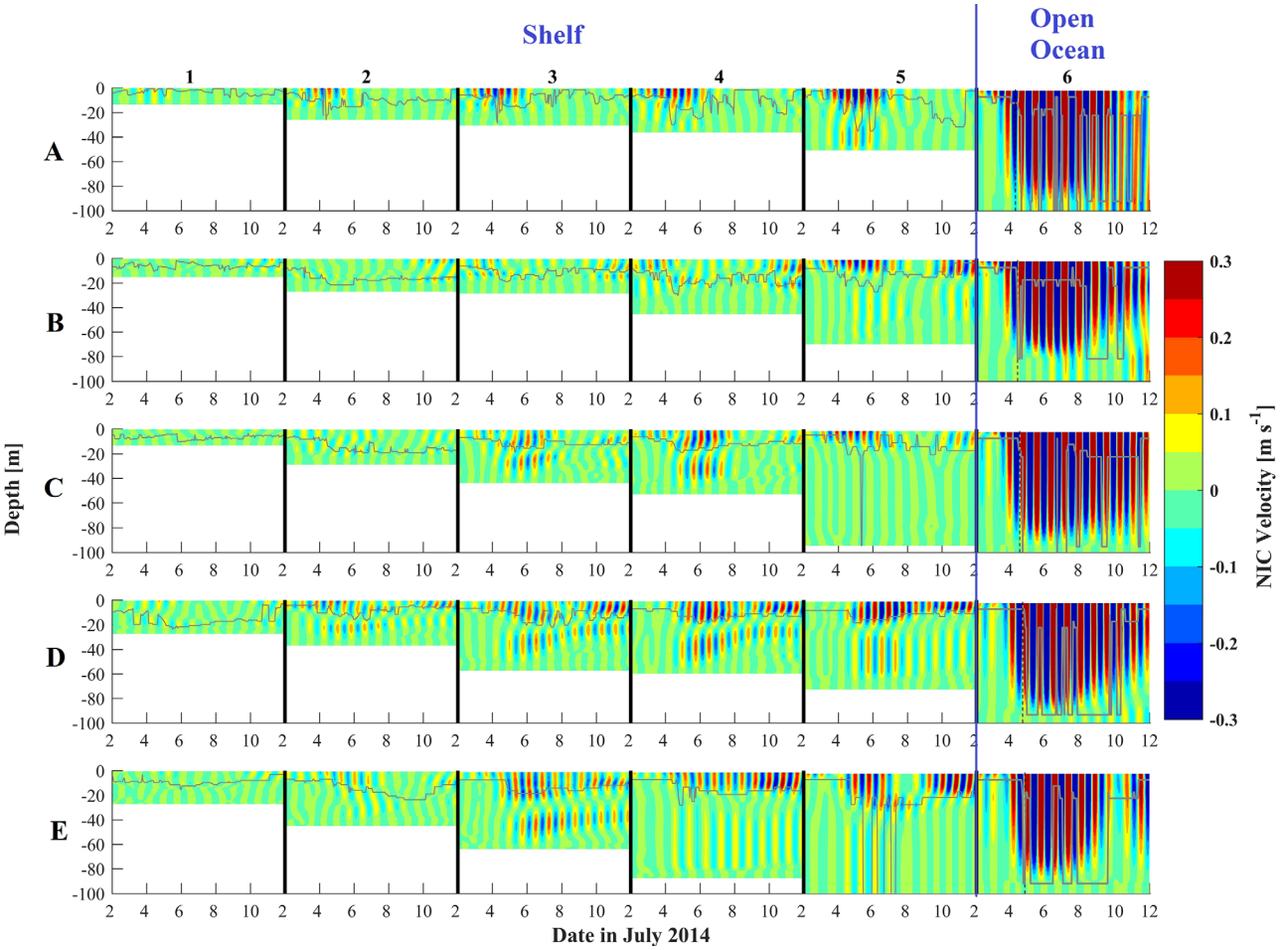

Figure 11. Time-depth distributions of NICs (cross-shelf component) along the 5 cross-shelf sections. The black dashed lines in column 6 indicate the passage of the storm's center, and the thin gray lines indicate the depth of maximum density gradient (the pycnocline separating the surface and bottom boundary layers).

water (e.g., Sanford et al., 2011). The currents were strongest near the ocean surface and decayed with depth. In contrast, the NICs on the shelf displayed a two-layer baroclinic structure. The upper-layer and lower-layer currents were separated at the pycnocline depth, indicating a mode-1 wave structure.

The NICs were weakest near the coast and got stronger in the offshore direction. This result is in agreement with Pettigrew's (1981) theoretical prediction based on a linear, two-layer, flat-bottom, cross-sectional model with a coastal wall boundary. He showed that a mode-1 current structure developed on the shelf and the current magnitude increased away from the coast. In addition to this strong cross-shelf variation, the detailed vertical structure of NICs varied among the stations and appeared to be set mainly by the vertical stratification profile. At the shallow sites such as C3–E3 and C4–D4, the surface and bottom layers were of similar depths such that the currents in the two layers were of comparable magnitude even though they always varied out of the phase. At the deeper shelf sites such as B5–E5 and E4, the surface mixed layer was much thinner than the bottom layer. Consequently, the currents were much stronger in the surface layer. Such differences are expected since the ratio of surface to bottom NICs was shown to be inversely proportional to the ratio of the layer depths (Millot & Crépon, 1981).

Figures 4 and 11 suggest that most of the NICs on the MAB shelf were mode-1 waves. To provide a quantitative description of the modal structure of the near-inertial waves, empirical orthogonal analysis was performed. The NICs were decomposed to five orthogonal vertical modes. The shape of each mode $\frac{d\psi_n(z)}{dz}$ (n = 1 to 5) is determined by the following equation:

$$\frac{\partial^2}{\partial z^2}\psi_n(z) = -\left[\frac{N^2(z)}{c_n^2}\right]\psi_n(z) \tag{6}$$

where $N(z)$ is buoyancy frequency, c_n is the eigenvelocity of each mode, and $\psi_n(z)=0$ at both the ocean surface and the sea floor (e.g., Alford & Zhao, 2007; MacKinnon & Gregg, 2005). $N(z)$ was averaged between 2 and 12 July. The eigenvalue and eigenvector of equation (6) are c_n and $\psi_n(z)$ for each vertical mode, respectively. The NICs velocity of each vertical mode was then obtained by fitting NICs vertical profiles to $\frac{d\psi_n(z)}{dz}$ of the first 5 modes with the least squares method, assuming no NICs at higher vertical modes. To assess the energy content in each mode, we calculate the percentage of the NICs kinetic energy in each mode (Figure 12):

$$P_n = \frac{<\int_{-H}^{0} KE_n>}{\sum_{n=1}^{5} <\int_{-H}^{0} KE_n>} \times 100\% \tag{7}$$

where $<>$ denotes the time-averaging between 2 and 12 July, the numerator denotes the kinetic energy in mode n, and the denominator denotes the sum of the kinetic energy in all the five modes. Overall, mode-1 contained 76% of the total kinetic energy in the near-inertial waves on the MAB shelf, mode-2 accounted for 12% (Figure 12), and the remainder was split among the three higher modes (not shown). In the cross-shelf direction, P_1 increased from ~60% in the near-shore region to over 80% near the shelf-break. In the

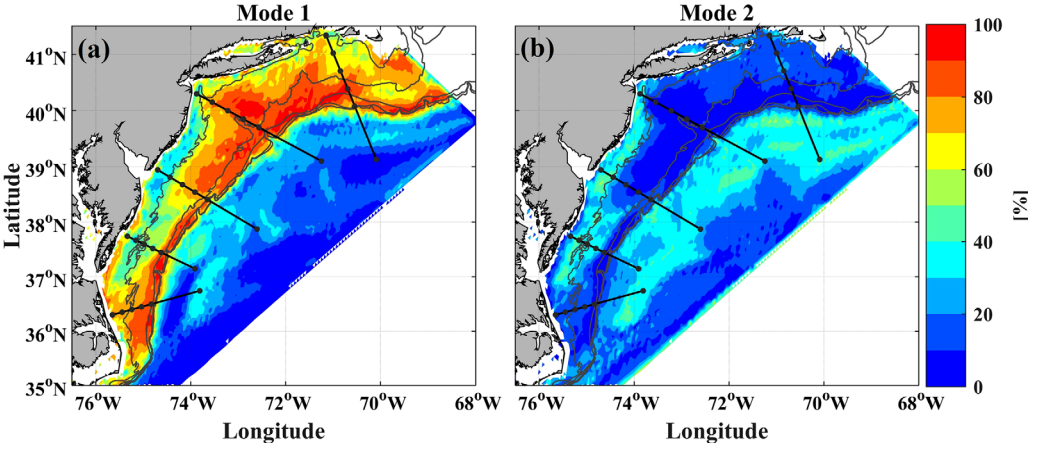

Figure 12. Percentage of the NICs kinetic energy in (a) mode-1 and (b) mode-2.

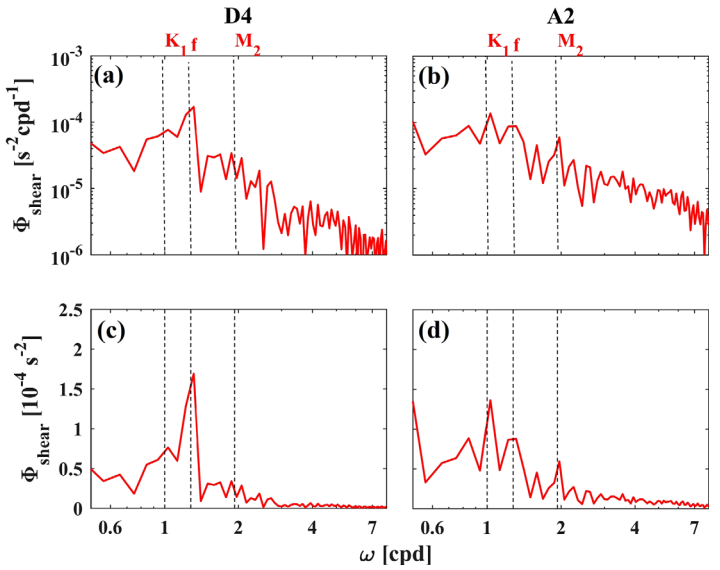

Figure 13. Depth-averaged shear spectra/variance-preserving spectra at (a, c) D4 and (b, d) A2.

shelf area between the mouths of Chesapeake and Delaware Bays (between 37°N and 38.5°N), P_1 decreased to 50% and P_2 increased to 40%, consistent with previous vertical profiles at B3 and B4 (second row in Figure 11).

5. Conclusion and Discussion

This paper presented a combined observational and modeling investigation into the near-inertial waves generated by Hurricane Arthur during its passage over the MAB. Both the HF radars and the numerical model showed that the NICs decreased substantially from the deep ocean to the MAB shelf. Due to the presence of a coastline as well as weaker wind stress away from the storm center, the NICs on the MAB shelf decreased onshore. The glider and the numerical model showed that the NICs had a two-layer baroclinic structure. The mode-1 near-inertial waves contained over 70% of the NICs kinetic energy over the MAB shelf.

Our findings of the mode-1 wave structure and onshore decrease of the NICs amplitude are consistent with previous observations (MacKinnon & Gregg, 2005; Shearman, 2005) and theoretical predictions (Kundu et al., 1983; Millot & Crépon, 1981; Pettigrew, 1981). In the mooring records collected in New England shelf, Shearman (2005) found that the mode-1 baroclinic structure was coherent across the entire shelf, with a magnitude that decreased onshore. Using a two-dimensional linear model of a flat-bottomed shelf, Pettigrew (1981) obtained a solution for the near-inertial currents and found that the mode-1 vertical structure was a result of a surface mixed layer response and barotropic wave emanating from the coastline. He also predicted that the NICs were zero at the coast and increased in the offshore direction.

Most of the NICs differences between the MAB shelf and the deep ocean appear to be related to the asymmetry of the wind energy input between the left and right sides of the storm track. The wind energy input was relatively high in the mid-to-outer shelf region between the New Jersey Coast and New England Shelf, which corresponds to higher *KE* than other shelf areas. In the southern MAB, the time-averaged *KE* was weak even though the wind energy input was large. The analysis of the energy budget showed that the large wind work was quickly balanced by the energy dissipation, which led to the rapid damping of the NICs there. In the northern MAB, however, the energy dissipation lagged the wind energy input such that the NICs persisted. When analyzing the mooring data collected on the New England Shelf, MacKinnon and Gregg (2005) also found that the wave evolution was controlled by the balance among wind stress, bottom drag, and turbulent dissipation.

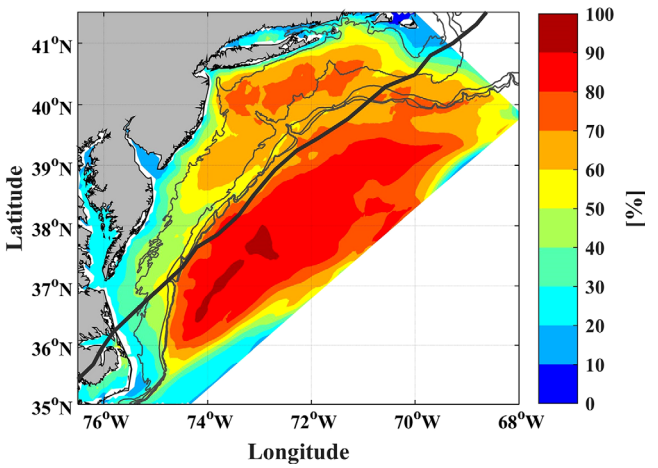

Figure 14. Percentage of the depth-averaged NICs-induced shear.

With a predominant mode-1 vertical structure, the strongest shear in the NICs usually coincides with the pycnocline (see Figure 11), thus making NICs a potentially important mechanism for generating turbulent mixing on the shelf. We computed the depth-averaged shear spectra at two stations: station A2 in the inner shelf of southern MAB and station D4 in the midshelf (Figure 13). At A2 where the storm center was closest to the coast, the highest peak is found around 1 d^{-1} frequency and is probably related to the strong wind-driven longshore currents. However, at D4, the NICs were the largest contributor to the shear spectrum. Figure 14 shows the ratio of the NICs-induced shear to the total current shear over the entire model domain. In the deep ocean, the NICs-induced shear accounted for over 80% of the total shear. On the MAB shelf, the NICs accounted for 60–80% of the shear on the New England shelf and 30–50% farther south on the MAB. The NICs only contributed to about 20% of the total shear in the inner shelf region off the Outer Banks. Since turbulent mixing may

cool the surface mixed layer and affect the storm intensity, it would be worthwhile to investigate the role of the NICs in generating mixing in a future study.

Acknowledgments
Funding support was provided by Maryland Sea grant (NA14OAR4170090, SA75281450-H) and the NOAA Cooperative Institute for the North Atlantic Region (CINAR, NA13OAR4830233), Disaster Recovery Act. Fan Zhang is supported by Maryland Sea Grant Fellowship and Travis Miles was supported by Teledyne Webb Research Graduate Fellowship. Suggestions from Xiaohui Xie are greatly appreciated. We thank the two reviewers for their helpful comments. HF radar data can be downloaded from http://tds.marine.rutgers.edu/thredds/catalog/cool/codar/totals/5Mhz_6km_realtime_fmrc/catalog.html?dataset=cool/codar/totals/5Mhz_6km_realtime_fmrc/Maracoos_5MHz_6km_Totals-FMRC_best.ncd. The glider data and WRF-FVCOM model outputs are available at https://zenodo.org/record/1208153#.WrpnTYjwZPZ. This is UMCES contribution 5484.

References

Alford, M. H., MacKinnon, J. A., Simmons, H. L., & Nash, J. D. (2016). Near-inertial internal gravity waves in the ocean. *Annual Review of Marine Science*, *8*, 95–123. https://doi.org/10.1146/annurev-marine-010814-015746

Alford, M. H., & Zhao, Z. (2007). Global patterns of low-mode internal-wave propagation. Part I: Energy and energy flux. *Journal of Physical Oceanography*, *37*(7), 1829–1848. https://doi.org/10.1175/JPO3085.1

Amante, C., & Eakins, B. W. (2009). *ETOPO1 Global Relief Model converted to PanMap layer format*. Boulder, CO: NOAA-National Geophysical Data Center.

Barrick, D. E. (1971a). Theory of HF and VHF propagation across the Rough Sea, 1, The effective surface impedance for a slightly rough highly conducting medium at grazing incidence. *Radio Science*, *6*(5), 517–526. https://doi.org/10.1029/RS006i005p00517

Barrick, D. E. (1971b). Theory of HF and VHF propagation across the Rough Sea, 2, Application to HF and VHF propagation above the sea. *Radio Science*, *6*(5), 527–533. https://doi.org/10.1029/RS006i005p00527

Belcher, S. E., Grant, A. L., Hanley, K. E., Fox-Kemper, B., Van Roekel, L., Sullivan, P. P., et al. (2012). A global perspective on Langmuir turbulence in the ocean surface boundary layer. *Geophysical Research Letters*, *39*, L18605. https://doi.org/10.1029/2012GL052932

Burchard, H. (2002). *Applied turbulence modelling in marine waters*. Berlin, Germany: Springer.

Burchard, H., & Bolding, K. (2001). Comparative analysis of four second-moment turbulence closure models for the oceanic mixed layer. *Journal of Physical Oceanography*, *31*(8), 1943–1968. https://doi.org/10.1175/1520-0485(2001)031<1943:CAOFSM>2.0.CO;2

Castelao, R., Glenn, S., & Schofield, O. (2010). Temperature, salinity, and density variability in the central Middle Atlantic Bight. *Journal of Geophysical Research*, *115*, C10005. https://doi.org/10.1029/2009JC006082

Chant, R. J. (2001). Evolution of near-inertial waves during an upwelling event on the New Jersey inner shelf. *Journal of Physical Oceanography*, *31*(3), 746–764. https://doi.org/10.1175/1520-0485(2001)031<0746:EONIWD>2.0.CO;2

Chen, C., Liu, H., & Beardsley, R. C. (2003). An unstructured grid, finite-volume, three-dimensional, primitive equations ocean model: Application to coastal ocean and estuaries. *Journal of Atmospheric and Oceanic Technology*, *20*, 159–186. https://doi.org/10.1175/1520-0426(2003)020<0159:AUGFVT>2.0.CO;2

Chen, C., Reid, R. O., & Nowlin, W. D. (1996). Near-inertial oscillations over the Texas-Louisiana shelf. *Journal of Geophysical Research*, *101*(C2), 3509–3524. https://doi.org/10.1029/95JC03395

Churchill, J. H., Wirick, C. D., Flagg, C. N., & Pietrafesa, L. J. (1994). Sediment resuspension over the continental shelf east of the Delmarva Peninsula. *Deep-Sea Research Part II*, *41*(2–3), 341–363. https://doi.org/10.1016/0967-0645(94)90027-2

Cuypers, Y., Le Vaillant, X., Bouruet-Aubertot, P., Vialard, J., & Mcphaden, M. J. (2013). Tropical storm-induced near-inertial internal waves during the Cirene experiment: Energy fluxes and impact on vertical mixing. *Journal of Geophysical Research: Oceans*, *118*, 358–380. https://doi.org/10.1029/2012JC007881

D'Asaro, E. A. (1985). The energy flux from the wind to near-inertial motions in the surface mixed layer. *Journal of Physical Oceanography*, *15*(8), 1043–1059. https://doi.org/10.1175/1520-0485(1985)015<1043:TEFFTW>2.0.CO;2

D'Asaro, E. A. (1995a). Upper-ocean inertial currents forced by a strong storm. Part II: Modeling. *Journal of Physical Oceanography*, *25*(11), 2937–2952. https://doi.org/10.1175/1520-0485(1995)025<2937:UOICFB>2.0.CO;2

D'Asaro, E. A. (1995b). Upper-ocean inertial currents forced by a strong storm. Part III: Interaction of inertial currents and mesoscale eddies. *Journal of Physical Oceanography*, *25*(11), 2953–2958. https://doi.org/10.1175/1520-0485(1995)025<2953:UOICFB>2.0.CO;2

D'Asaro, E. A., Eriksen, C. C., Levine, M. D., Paulson, C. A., Niiler, P., & Van Meurs, P. (1995). Upper-ocean inertial currents forced by a strong storm. Part I: Data and comparisons with linear theory. *Journal of Physical Oceanography*, *25*(11), 2909–2936. https://doi.org/10.1175/1520-0485(1995)025 < 2909:UOICFB>2.0.CO;2

D'Asaro, E. A., Sanford, T. B., Niiler, P. P., & Terrill, E. J. (2007). Cold wake of hurricane Frances. *Geophysical Research Letters*, *34*, L15609. https://doi.org/10.1029/2007GL030160

Egbert, G. D., & Erofeeva, S. Y. (2002). Efficient inverse modeling of barotropic ocean tides. *Journal of Atmospheric and Oceanic Technology*, *19*(2), 183–204. https://doi.org/10.1175/1520-0426(2002)019<0183:EIMOBO>2.0.CO;2

Fleming, N. E. (2016). *Seasonal and spatial variability in temperature, salinity and circulation of the Middle Atlantic Bight* (PhD thesis). New Brunswick, NJ: Rutgers The State University of New Jersey-New Brunswick.

Gill, A. E. (1984). On the behavior of internal waves in the wakes of storms. *Journal of Physical Oceanography*, *14*(7), 1129–1151. https://doi.org/10.1175/1520-0485(1984)014<1129:OTBOIW>2.0.CO;2

Glenn, S. M., Miles, T. N., Seroka, G. N., Xu, Y., Forney, R. K., Yu, F., et al. (2016). Stratified coastal ocean interactions with tropical cyclones. *Nature Communications*, *7*, 10887. https://doi.org/10.1038/ncomms10887

Houghton, R. W., Schlitz, R., Beardsley, R. C., Butman, B., & Chamberlin, J. L. (1982). The Middle Atlantic Bight cold pool: Evolution of the temperature structure during summer 1979. *Journal of Physical Oceanography*, *12*(10), 1019–1029. https://doi.org/10.1175/1520-0485(1982)012<1019:TMABCP>2.0.CO;2

Kohut, J., Roarty, H., Randall-Goodwin, E., Glenn, S., & Lichtenwalner, C. S. (2012). Evaluation of two algorithms for a network of coastal HF radars in the Mid-Atlantic Bight. *Ocean Dynamics*, *62*(6), 953–968. https://doi.org/10.1007/s10236-012-0533-9

Kundu, P. K., Chao, S. Y., & McCreary, J. P. (1983). Transient coastal currents and inertio-gravity waves. *Deep-Sea Research Part A*, *30*(10), 1059–1082. https://doi.org/10.1016/0198-0149(83)90061-4

Lee, S. B., Li, M., & Zhang, F. (2017). Impact of sea level rise on tidal range in Chesapeake and Delaware Bays. *Journal of Geophysical Research: Oceans*, *122*, 3917–3938. https://doi.org/10.1002/2016JC012597

Lentz, S. J. (2017). Seasonal warming of the Middle Atlantic Bight Cold Pool. *Journal of Geophysical Research: Oceans*, *122*, 941–954. https://doi.org/10.1002/2016JC012201

Lentz, S., Carr, M., & Herbers, T. H. C. (2001). Barotropic tides on the North Carolina shelf. *Journal of Physical Oceanography*, *31*(7), 1843–1859. https://doi.org/10.1175/1520-0485(2001)031<1843:BTOTNC>2.0.CO;2

MacKinnon, J. A., & Gregg, M. C. (2005). Near-inertial waves on the New England shelf: The role of evolving stratification, turbulent dissipation, and bottom drag. *Journal of Physical Oceanography*, *35*(12), 2408–2424. https://doi.org/10.1175/JPO2822.1

Mellor, G. L. (2001). One-dimensional, ocean surface layer modeling: A problem and a solution. *Journal of Physical Oceanography*, *31*(3), 790–809. https://doi.org/10.1175/1520-0485(2001)031<0790:ODOSLM>2.0.CO;2

Miles, T., Glenn, S. M., & Schofield, O. (2013). Temporal and spatial variability in fall storm induced sediment resuspension on the Mid-Atlantic Bight. *Continental Shelf Research*, *63*, S36–S49. https://doi.org/10.1016/j.csr.2012.08.006

Miles, T., Seroka, G., & Glenn, S. (2017). Coastal ocean circulation during Hurricane Sandy. *Journal of Geophysical Research: Oceans*, *122*, 7095–7114. https://doi.org/10.1002/2017JC01303

Miles, T., Seroka, G., Kohut, J., Schofield, O., & Glenn, S. (2015). Glider observations and modeling of sediment transport in Hurricane Sandy. *Journal of Geophysical Research: Oceans*, *120*, 1771–1791. https://doi.org/10.1002/2014JC010474

Millot, C., & Crépon, M. (1981). Inertial oscillations on the continental shelf of the Gulf of Lions-Observations and theory. *Journal of Physical Oceanography*, *11*(5), 639–657.

Pettigrew, N. R. (1981). *The dynamics and kinematics of the coastal boundary layer off Long Island (PhD thesis)*. Woods Hole, MA: Woods Hole Oceanography Institution.

Pollard, R. T. (1980). Properties of near-surface inertial oscillations. *Journal of Physical Oceanography*, *10*(3), 385–398. https://doi.org/10.1175/1520-0485(1980)010<0385:PONSIO>2.0.CO;2

Pollard, R. T., & Millard, R. C. (1970). Comparison between observed and simulated wind-generated inertial oscillations. *Deep Sea Research and Oceanographic Abstracts*, *17*(4), 153–175. https://doi.org/10.1016/0011-7471(70)90043-4

Price, J. F. (1983). Internal wave wake of a moving storm. Part I. Scales, energy budget and observations. *Journal of Physical Oceanography*, *13*(6), 949–965. https://doi.org/10.1175/1520-0485(1983)013<0949:IWWOAM>2.0.CO;2

Price, J. F., Sanford, T. B., & Forristall, G. Z. (1994). Forced stage response to a moving hurricane. *Journal of Physical Oceanography*, *24*(2), 233–260. https://doi.org/10.1175/1520-0485(1994)024<0233:FSRTAM>2.0.CO;2

Roarty, H., Glenn, S., Kohut, J., Gong, D., Handel, E., Rivera, E., et al. (2010). Operation and application of a regional high-frequency radar network in the Mid-Atlantic Bight. *Marine Technology Society Journal*, *44*(6), 133–145. https://doi.org/10.4031/MTSJ.44.6.5

Sanford, T. B., Price, J. F., & Girton, J. B. (2011). Upper-ocean response to Hurricane Frances (2004) observed by profiling EM-APEX floats. *Journal of Physical Oceanography*, *41*(6), 1041–1056. https://doi.org/10.1175/2010JPO4313.1

Sanford, T. B., Price, J. F., Girton, J. B., & Webb, D. C. (2007). Highly resolved observations and simulations of the ocean response to a hurricane. *Geophysical Research Letters*, *34*, L13604. https://doi.org/10.1029/2007GL029679

Seroka, G., Miles, T., Xu, Y., Kohut, J., Schofield, O., & Glenn, S. (2016). Hurricane irene sensitivity to stratified coastal ocean cooling. *Monthly Weather Review*, *144*(9), 3507–3530. https://doi.org/10.1175/MWR-D-15-0452.1

Seroka, G., Miles, T., Xu, Y., Kohut, J., Schofield, O., & Glenn, S. (2017). Rapid shelf-wide cooling response of a stratified coastal ocean to hurricanes. *Journal of Geophysical Research: Oceans*, *122*, 4845–4867. https://doi.org/10.1002/2017JC012756

Shearman, R. K. (2005). Observations of near-inertial current variability on the New England shelf. *Journal of Geophysical Research*, *110*, C02012. https://doi.org/10.1029/2004JC002341

Teague, C. C. (1971). *High frequency resonant scattering techniques for the observation of directional ocean wave spectra*. Stanford, CA: Department of Electrical Engineering, Stanford University.

Warner, J. C., Sherwood, C. R., Arango, H. G., & Signell, R. P. (2005). Performance of four turbulence closure models implemented using a generic length scale method. *Ocean Modelling*, *8*(1), 81–113. https://doi.org/10.1016/j.ocemod.2003.12.003

Zhai, X., Greatbatch, R. J., Eden, C., & Hibiya, T. (2009). On the loss of wind-induced near-inertial energy to turbulent mixing in the upper ocean. *Journal of Physical Oceanography*, *39*(11), 3040–3045. https://doi.org/10.1175/2009JPO4259.1

Zhang, F., Li, M., Ross, A. C., Lee, S. B., & Zhang, D.-L. (2017). Sensitivity analysis of Hurricane Arthur (2014) storm surge forecasts to WRF physics parameterizations and model configurations. *Weather and Forecasting*, *32*(5), 1745–1764. https://doi.org/10.1175/WAF-D-16-0218.1